High-Performance Electrocatalysis for Hydrogen Evolution Reaction Using Se-Doped Pyrite-Phase Nickel Diphosphide Nanostructures

ARTICLE *in* ACS CATALYSIS · SEPTEMBER 2015

Impact Factor: 9.31 · DOI: 10.1021/acscatal.5b01657

Article

High-Performance Electrocatalysis for Hydrogen Evolution Reaction Using Se-Doped Pyrite-Phase Nickel Diphosphide Nanostructures

Junqiao Zhuo, Miguel Cabán-Acevedo, Hanfeng Liang, Leith Samad, Qi Ding, Yongping Fu, Meixian Li, and Song Jin

ACS Catal., **Just Accepted Manuscript** • DOI: 10.1021/acscatal.5b01657 • Publication Date (Web): 16 Sep 2015

High-Performance Electrocatalysis for Hydrogen Evolution Reaction Using Se-Doped Pyrite-Phase Nickel Diphosphide Nanostructures

Junqiao Zhuo,[†,‡] *Miguel Cabán-Acevedo*,[†] *Hanfeng Liang*,[†,#] *Leith Samad*,[†] *Qi Ding*,[†] *Yongping Fu*,[†] *Meixian Li*,[*,‡] *and Song Jin*[*,†]

[†]Department of Chemistry, University of Wisconsin–Madison, 1101 University Avenue, Madison, Wisconsin 53706, United States; [‡]Institute of Analytical Chemistry, College of Chemistry and Molecular Engineering, Peking University, Beijing 100871, P.R. China; [#]College of Chemistry and Chemical Engineering, Xiamen University, Xiamen 361005, P.R. China.

[*]E-mail: jin@chem.wisc.edu

KEYWORDS: hydrogen evolution reaction (HER); nickel diphosphide (NiP_2); nickel diselenide ($NiSe_2$); electrocatalysis; doping; pyrite-phase

ABSTRACT

The study of efficient, robust, and earth-abundant electrocatalysts for the hydrogen evolution reaction (HER) is essential for hydrogen-based energy technologies. Previous works have demonstrated that pyrite-structure materials (e.g. CoS_2, $NiSe_2$) are efficient HER catalysts. Here we first systematically investigate the nanostructure synthesis of a series of pyrite-phase nickel phosphoselenide materials: NiP_2, Se-doped NiP_2 ($NiP_{1.93}Se_{0.07}$), P-doped $NiSe_2$ ($NiP_{0.09}Se_{1.91}$), and $NiSe_2$ through a facile thermal conversion of $Ni(OH)_2$ nanoflakes. The similar nanostructures enable a systematic and fair comparison of their structural properties and catalytic activities for HER. We found that $NiP_{1.93}Se_{0.07}$ shows the best HER performance, followed by NiP_2, $NiP_{0.09}Se_{1.91}$, and $NiSe_2$. Se-doped NiP_2 grown on carbon fiber paper can achieve an electrocatalytic current density of 10 mA cm^{-2} at an overpotential as low as 84 mV and a small Tafel slope of 41 mV $decade^{-1}$. This study not only estabilishes Se-doped NiP_2 as a competitive HER catalyst, but also demonstrates that doping or alloying of developed catalysts (especially doping with anions from another group, e.g. selenium to phosphorus) can improve the HER catalytic activity, which provides a general strategy to improve catalytic efficiencies of existing electrocatalysts for HER.

INTRODUCTION

With the rapid consumption of fossil fuels and serious environmental problems, hydrogen is proposed as a renewable, secure, and clean alternative energy source[1,2] and electrocatalysis of water driven by solar energy is an attractive and promising method to produce hydrogen.[3-5] The study of catalysts for the hydrogen evolution reaction (HER) aims to decrease the electrochemical overpotential and improve the efficiency in energy conversion and has attracted a great deal of interest.[6] Noble metals, such as Pt, show high catalytic activity, however, their high cost and scarcity seriously limit their feasibility in large scale production. Therefore, the exploration of highly efficient and low-cost electrocatalysts for HER has witnessed significant recent developments.[6-9] Several families of earth-abundant materials including transition metal sulfides,[10-23] selenides,[22,24-29] nitrides,[30,31] phosphides,[32-42] and borides[43,44] have been shown to be promising electrocatalysts for HER. Among the reported materials, the cubic pyrite-phase transition metal dichalcogenides (e.g. FeS_2, CoS_2, NiS_2, $CoSe_2$, and $NiSe_2$) have been identified as a family of very promising earth-abundant and low-cost HER catalysts (and electrocatalysts for other reduction reactions[20,45]) that are not only very efficient but also stable in both acidic and basic solutions.[19-22,28] Some works have attributed the excellent catalytic activity to the particular role of disulfide (S_2^{2-}) (or dichalcogenide) dumbbell anions in pyrite or other chalcogenides in catalyzing HER.[20,46-48]

Very recently, we have identified ternary pyrite-type compound cobalt phosphosulfide (CoPS) as a new HER electrocatalyst with an exceptionally high activity.[49] In comparison to the parent pyrite structure CoS_2, the substitution of a sulfur atom in the chalcogenide dumbbell with phosphorus in CoPS could tune the electronic structure of the electrocatalyst and shift the hydrogen absorption free energy closer to thermal neutral, and thus result in superior catalytic

performance. In addition, pyrite-phase nickel diphosphide (NiP_2) was reported as a high-pressure phase 40 years ago.[50] Recently, there are reports on pyrite-phase NiP_2[37] and $NiSe_2$[21,22] as catalysts for HER. Note that among the various nickel phophides that display good HER catalytic activity,[33,35,37,42,51] only NiP_2 has the pyrite structure. Building upon these discoveries, we hypothesize that the synthesis of ternary pyrite-type metal phosphosulfides or phosphoselenides by means of alloying or doping could serve as a general strategy to improve catalytic HER activity building on top of promising binary metal pyrites.

A variety of strategies have been used to improve the performance of electrocatalysts for HER[6,9,15] such as nanostructuring,[10,19,35,39] structural modification,[14,17,18] and modification of chemical composition.[20,21,52-55] Doping with cations or anions could modify the electronic structure and optimize the hydrogen adsorption energy,[52-55] which is an important and useful approach to improve the intrinsic activity of catalysts. Doping or alloying between metal elements has been more commonly studied,[6,20,21] but mixing non-metal elements usually would lead to more significant modification of electronic structure and thus catalytic activity. For example, $MoS_{2(1-x)}Se_{2x}$ was reported to show better HER catalytic performance than MoS_2 and $MoSe_2$.[53] Similar phenomena were also observed for $WS_{2(1-x)}Se_{2x}$ when compared with WS_2 and WSe_2.[55] Doping or alloying with non-metal elements from different groups, such as phosphorus to sulfur[36] or chlorine to sulfur[54], is expected to result in significant tuning of the electronic structures.

In this work, we systematically investigated the synthesis of pyrite-phase nickel phosphoselenides and prepared a series of NiP_2, Se-doped NiP_2, P-doped $NiSe_2$, and $NiSe_2$ nanostructures through thermal conversion of $Ni(OH)_2$ precursor nanostructures in appropriate P and/or Se vapors. This facile synthetic method makes it convenient to systematically compare the

structural property and catalytic activity for HER and establish the relationship between synthesis, structure, and catalytic activity. We found that the doping of NiP_2 with Se not only reduced the overpotential, but also decreased the Tafel slope and increased exchange current density, thus significantly improving the HER catalytic performance. Se-doped NiP_2 ($NiP_{1.93}Se_{0.07}$) is a highly active and stable electrocatalyst for HER and shows the best performance among the four pyrite-phase compounds, followed by NiP_2, P-doped $NiSe_2$ ($NiP_{0.09}Se_{1.91}$), and $NiSe_2$. Se-doped NiP_2 ($NiP_{1.93}Se_{0.07}$) grown on carbon fiber paper can achieve a catalytic current density of 10 mA cm^{-2} at an overpotential of 84 mV with a Tafel slope of 41 mV $decade^{-1}$, which estabilishes $NiP_{1.93}Se_{0.07}$ as a highly-active, earth-abundant, and stable electrocatalyst for the HER.

EXPERIMENTAL SECTION

All chemicals were purchased from Sigma-Aldrich and used without further purifications unless otherwise noted.

Synthesis of Electrocatalyst Materials.

$Ni(OH)_2$ nanoflake precursor. Nickel hydroxide hydrate ($Ni(OH)_2 \cdot 0.75H_2O$) nanoflakes were synthesized on graphite disks and carbon fiber paper electrodes by modifying a reported procedure for synthesizing cobalt hydroxide nanostructure analogs.[19] Additional details of the electrode preparation are in the Supporting Information. 6 mmol of $Ni(NO_3)_2 \cdot 6H_2O$ (≥ 98.5%), 12 mmol NH_4F (≥ 98.0%), and 30 mmol $(NH_2)_2CO$ (99.5–100.5%) were dissolved in 200 mL of 18.2 MΩ de-ionized water. 16 mL of the solution was transferred to a 23-mL PTFE-lined stainless steel autoclave containing the substrate leaned against the autoclave wall (see Figure S1

for details of this setup). After the sealed autoclave was heated at 110 °C for 3 h, it was cooled down. Then the substrate was removed, washed with water and ethanol, and dried in an oven at 80 °C for 20 min.

Thermal conversion. The graphite or carbon paper substrates covered with the nanoflakes were placed in the center of a fused silica tube in a Lindberg/Blue M tube furnace equipped with both pressure regulators and gas flow controllers. An alumina boat containing a total of 10 mmol of phosphorous (99.5–100.5%) and selenium (99.5–100.5%) powders with varying ratios (pure P, 3:1, 3:2, 3:3, 2:3, pure Se) was placed at the farthest upstream position within the reactor tube. The tube was purged 3 times with Argon and maintained at 780 Torr under a steady flow of Ar carrier gas (99.999%) at 25 sccm. The furnace temperature was ramped to 500 °C and held for 30 min. After cooling under Ar flow, the samples were removed and rinsed with CS_2 (99.9%) for 10 min, then washed with ethanol, and dried in a flow of N_2 gas.

Structural Characterization.

Scanning electron microscope (SEM) and energy dispersive X-ray spectroscopy (EDS) were performed using a LEO SUPRA 55 VP field-emission SEM with EDS capabilities. The voltages for SEM imaging and EDS mapping were 3 keV and 15 keV, respectively. Raman spectra were collected on a Horiba Jobin Yvon Labram Aramis Confocal Raman microscope with a 532 nm laser and ~16 μm diameter laser spot size. Powder X-ray diffraction (PXRD) data were acquired on a Bruker D8 ADVANCE powder X-ray diffractometer equipped with a Cu Kα source. The transmission electron microscopy (TEM) samples were prepared by immersing and sonicating the samples grown on graphite disk in ethanol for 30 s, and drop-casting the suspension onto Cu TEM grids with lacey carbon support (Ted Pella, #01890-F). TEM images were taken on an FEI

Titan aberration-corrected scanning transmission electron microscope operated at an accelerating voltage of 200 kV in TEM mode.

Electrochemical Characterization.

All electrochemical measurements were conducted in a three-electrode setup with a rotating disk electrode (RDE, Bioanalytical Systems, Inc.; RDE-2) using a Bio-Logic SP-200 potentiostat. The measurements were performed in 0.5 M H_2SO_4(aq) electrolyte continuously purged with H_2(*g*) (99.999%), with a saturated calomel reference electrode (SCE) (CH Instruments), a graphite rod (National Carbon Co., AGKSP Spectroscopic Electrode) counter electrode, and a graphite disk or carbon fiber paper supported sample affixed to a glassy carbon RDE tip using silver paint (Ted Pella, PELCO Colloidal Silver) as the working electrode. Linear sweep voltammetry (LSV) measurements were performed at a scan rate of 3 mV s^{-1} while rotating the working electrode at 1000 RPM. The SCE was calibrated against the reversible hydrogen potential (RHE) using platinum wire (Kurt J. Lesker, 99.99%; 0.50 mm diameter) as both the working and counter electrodes in 0.5 M H_2SO_4 (E (RHE) = E (SCE) + 0.268 V). All measurements were corrected for a small ohmic loss (< 3.5 Ω) determined via impedance spectroscopy. Electrochemical impedance spectroscopy was performed in potentiostatic mode at −0.13 V vs. RHE with an applied sinusoidal voltage with an amplitude of 10 mV and scanning frequency from 200 kHz to 100 mHz. The data were fitted using a simplified Randles equivalent circuit (shown in Figure S2) to investigate the electrode kinetics. To determine the double-layer capacitance (C_{dl}) for each electrode, two CV cycles were recorded from 100 mV to 200 mV vs. RHE at scan rates of 40, 60, 80, 100, and 120 mV s^{-1}. Then, for each scan rate, ΔJ was measured at 150 mV vs. RHE and plotted against the scan rate. These data were then fit to a line, the slope of which is equal to twice the geometric C_{dl}.

RESULTS AND DISCUSSION

We prepared NiP_2, $NiSe_2$, and various $NiP_{2-x}Se_x$ nanostructures by thermal conversion of precursor $Ni(OH)_2$ nanostructures in different P and Se vapor environments (see details in Experimental Section). The precursor $Ni(OH)_2$ nanoflakes (typical images shown in Figure S3) were grown directly on conductive graphite disk (or carbon paper) substrates using a solution growth method (Figure S1).[19,56] Then, a total of 10 mmol of P and Se powders with varying ratios were mixed in a crucible, evaporated in the tube reactor at approximately 250 °C, and reacted with the as-prepared $Ni(OH)_2$ nanoflakes at 500 °C for 30 min in Ar atmosphere. Figure 1 shows the PXRD patterns of the products at different *n*(P) and *n*(Se) ratios (3:1, 3:2, 3:3, 2:3) compared with pure NiP_2 (3:0) and $NiSe_2$ (0:3) synthesized in pure P or Se environment under the same conditions. Both NiP_2 and $NiSe_2$ synthesized under these conditions are the cubic pyrite-structure phase (NiP_2, JCPDS 21-0590, space group $Pa\bar{3}$, a = 5.471 Å; $NiSe_2$, JCPDS 65-1843, space group $Pa\bar{3}$, a = 5.960 Å). The observed peak shifts of the samples converted with mixed precursors when compared with NiP_2 and $NiSe_2$ indicate the successful doping of NiP_2 with Se or $NiSe_2$ with P that causes the expansion or contraction of the crystal lattice, respectively. It is interesting that when *n*(P) was larger than *n*(Se), such as 3:2 and 3:1, NiP_2-like compounds ($NiP_{2-x}Se_x$, x is small) were formed (Figure 1a); when *n*(Se) was equal or larger than *n*(P), $NiSe_2$-like compounds were formed (Figure 1b). For Se-doped NiP_2, the peaks shift to smaller 2-θ angles compared with NiP_2 (Figure 1a inset), which suggests the expansion of the crystal lattice caused by the larger radius of Se compared with P. The opposite effect was observed in P-doped $NiSe_2$ when compared with $NiSe_2$ (Figure 1b inset). Using Vegard's law, we calculated the chemical compositions of the samples based on the observed peak shifts: for the sample prepared with a ratio of *n*(P) : *n*(Se) = 3:2, the composition was $NiP_{1.93}Se_{0.07}$; for the

sample prepared with a ratio of n(P) : n(Se) = 1:1 the composition was $NiP_{0.09}Se_{1.91}$. Interestingly, it seemed to be quite difficult to prepare nickel phosphoselenide product with a P:Se stoichiometry close to 1:1 (i.e. NiPSe) throughout the whole range of the P/Se precursor ratios employed, and the conversion products are either close to NiP_2 (when P/Se ratio > 1) or close to $NiSe_2$ (when P/Se ratio ≤ 1). This behavior is different from the case of cobalt phosphosulfide in which nearly stoichiometric CoPS can be readily formed.[49] This result is consistent with the previously reported *high pressure* synthesis of NiPSe, which reported two alloy phases of NiPSe consisting of $NiP_{1.86}Se_{0.14}$ and $NiP_{0.24}Se_{1.76}$.[57] Previous report and our own work demonstrate that it is difficult to synthesize the stoichiometric ternary compound of NiPSe.

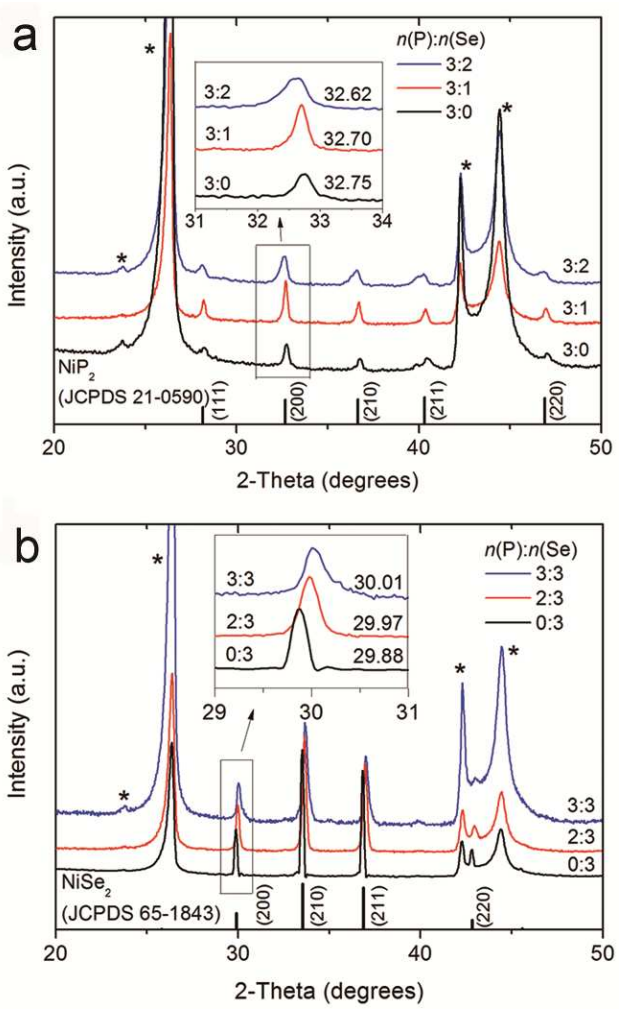

Figure 1. PXRD patterns of (a) NiP_2 and $NiP_{2-x}Se_x$ prepared at n(P):n(Se) = 3:2 and 3:1, (b) $NiSe_2$ and NiP_xSe_{2-x} prepared at n(P) : n(Se) = 2:3 and 3:3. The stars mark the diffraction peaks from the graphite disk substrate.

In the remaining discussion, we will focus on four representative samples: NiP_2, $NiP_{1.93}Se_{0.07}$, $NiP_{0.09}Se_{1.91}$, and $NiSe_2$. We also examined the influence of the reaction temperature on the conversion for the precursor ratio of n(P) : n(Se) = 3:2, as shown in Figure S4 in the Supporting Information. At 400 ^oC, the peaks were very weak, which may be caused by the incomplete conversion and poor crystallinity of the product. At 500 and 600 ^oC, there were strong peaks and all of the peaks shifted. However, the variations in the peak shifts from the sample prepared at 600 ^oC (Figure S4c) indicate the conversion at 600 ^oC is not as consistent. Finally, we chose 500 ^oC as the optimized conversion temperature.

The morphologies of NiP_2, $NiP_{1.93}Se_{0.07}$, $NiP_{0.09}Se_{1.91}$, and $NiSe_2$ were characterized by scanning electron microscope (SEM) and transmission electron microscopy (TEM) as shown in Figure 2. Both NiP_2 and $NiP_{1.93}Se_{0.07}$ are microflakes comprised of nanoparticles around 10 nm in diameter. In comparison, $NiP_{0.09}Se_{1.91}$ and $NiSe_2$ form larger microparticles with ~500 nm diameter. The difference in the particle size and morphology between the NiP_2 or doped NiP_2 and $NiSe_2$ or doped $NiSe_2$ is noticeable, which is likely due to the different crystal grow behaviors during the conversion reactions. The energy dispersive X-ray spectroscopy (EDS) spectra proved the nanoflakes were composed of Ni, P, and Se (Figure 3a). Also, elemental mapping images showed that the distribution of Ni, P, and Se atoms in the nanoflakes was homogeneous (Figure 3b and Figure S5 in the Supporting Information), which is consistent with the PXRD result and further confirms the composition.

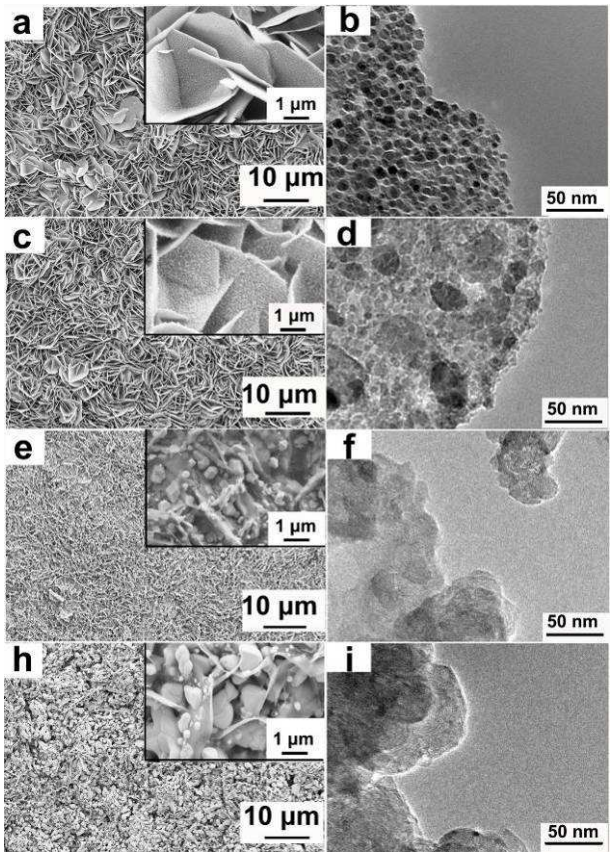

Figure 2. SEM and TEM images of the (a, b) NiP_2, (c, d) $NiP_{1.93}Se_{0.07}$, (e, f) $NiP_{0.09}Se_{1.91}$, and (h, i) $NiSe_2$ nanostructures.

Furthermore, Raman spectroscopy was employed to confirm the formation of pure and doped pyrite-phase products (Figure 3c). Typical pyrite-structure compounds show two peaks corresponding to X_2 (X = S, Se, P) libration (E_g) and in-phase stretch (A_g) for the X-X dumbbells.[20,58,59] The sharp peak in $NiSe_2$ at 205 cm^{-1} corresponds to the Se-Se stretching mode of cubic $NiSe_2$, while NiP_2 shows two peaks at 286 and 454 cm^{-1}, all of which are in agreement with what was reported for pyrites.[22,26,58,59] The Raman spectra of $NiP_{1.93}Se_{0.07}$ and $NiP_{0.09}Se_{1.91}$ are quite similar to those of NiP_2 and $NiSe_2$, respectively, which further confirms the pyrite structure and doping. The Raman peak positions also confirm that formation of pure or alloy phase of NiP_2 for the bottom two samples without impurity phases close to $NiSe_2$, and the

formation of pure or alloy phase of $NiSe_2$ for the top two samples without impurity phases close to NiP_2.

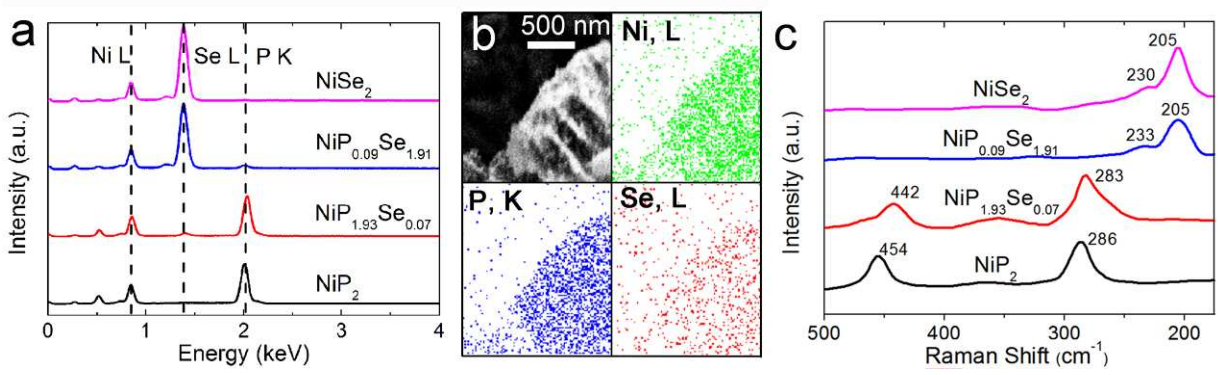

Figure 3. (a) EDS spectra of NiP_2, $NiP_{1.93}Se_{0.07}$, $NiP_{0.09}Se_{1.91}$, and $NiSe_2$ samples. (b) EDS mapping of $NiP_{1.93}Se_{0.07}$. (c) Raman spectra of NiP_2, $NiP_{1.93}Se_{0.07}$, $NiP_{0.09}Se_{1.91}$, and $NiSe_2$ samples.

The electrocatalytic HER activities of NiP_2, $NiP_{1.93}Se_{0.07}$, $NiP_{0.09}Se_{1.91}$, and $NiSe_2$ nanostructures were measured using a standard three-electrode setup in 0.5 M H_2SO_4 (aq) with continuously purging H_2. The graphite disks with samples were adhered on the glassy carbon working electrode of standard RDE apparatus by silver paint. It is worth noting that graphite disk and silver paint were inactive for HER and it was very convenient to perform characterizations on it. In addition, the direct growth of nanostructures on graphite disk ensures the good electrical contact between the substrate and the electrocatalysts. All data were *iR* corrected and the ohmic losses were always < 3.5 Ω. The polarization curves (Figure 4a) show the overpotentials needed for NiP_2, $NiP_{1.93}Se_{0.07}$, $NiP_{0.09}Se_{1.91}$, and $NiSe_2$ to achieve a catalytic current density of 10 mA cm^{-2} are 135, 102, 167, and 173 mV vs reversible hydrogen potential (RHE), respectively. The corresponding Tafel plots (Figure 4b) show all the Tafel plots can be well described with the Tafel equation in a relatively wide range (approximately 70 mV). The Tafel slopes of NiP_2,

$NiP_{1.93}Se_{0.07}$, $NiP_{0.09}Se_{1.91}$, and $NiSe_2$ are calculated to be 48, 42, 44, 31 mV decade^{-1}, respectively.

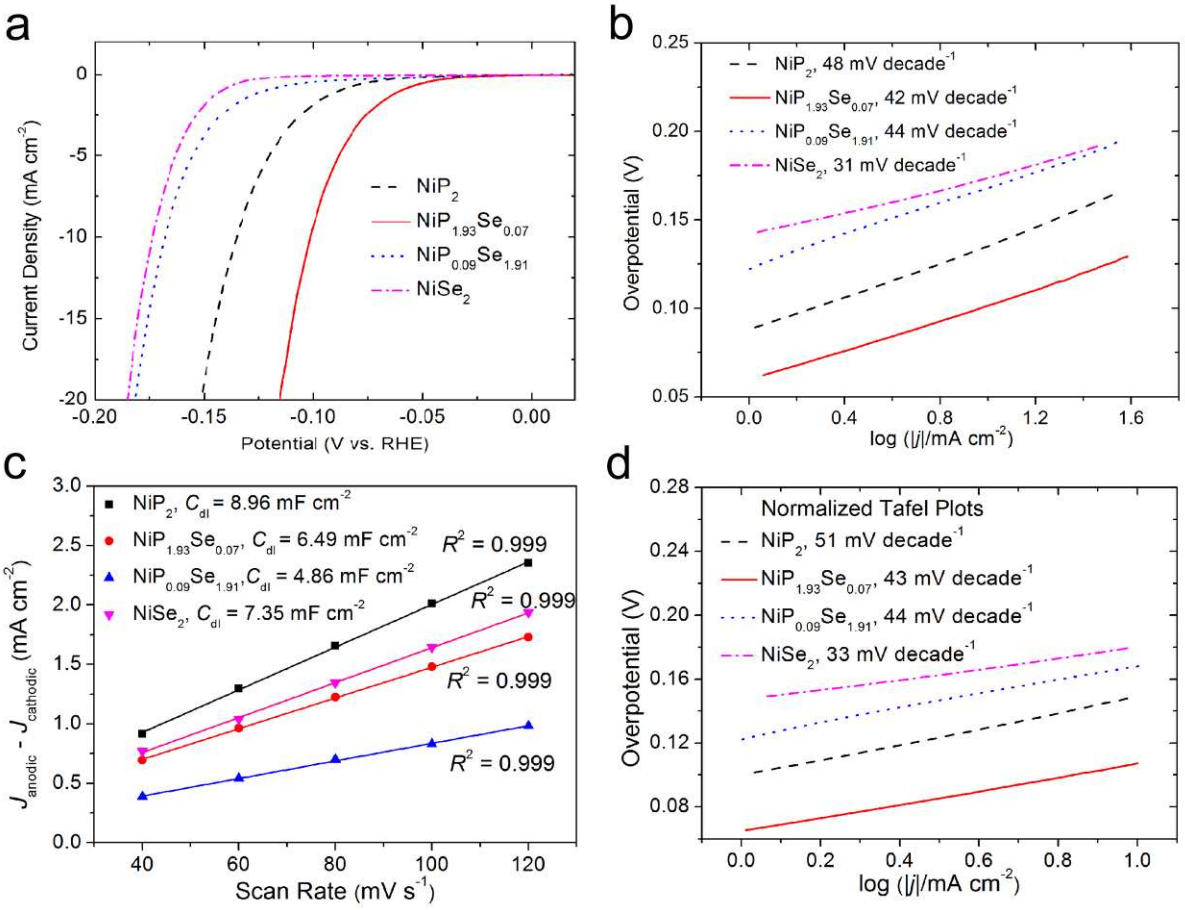

Figure 4. Electrochemical characterizations of NiP_2, $NiP_{1.93}Se_{0.07}$, $NiP_{0.09}Se_{1.91}$, and $NiSe_2$ nanostructures on graphite disk for HER electrocatalysis in 0.5 M H_2SO_4. (a) Polarization curves, (b) the corresponding Tafel plots, (c) the plots showing the extraction of the double-layer capacitance (C_{dl}), and (d) surface area normalized Tafel plots.

Although these samples were all converted from the same $Ni(OH)_2$ precursor nanostructures and have similar morphologies and surface areas, there were still some variations between samples. In order to compare them in a more meaningful fashion, we carried out cyclic

voltammetry (CV) scans to determine the double-layer capacitance (C_{dl}) (Figure 4c), which can be used to estimate the relative electrochemically active surface area assuming that the two are linearly proportional.[19,60] Using such relative surface areas, we can normalize the electrochemical data to determine the normalized Tafel slope and normalized exchange current density.[19,49] The geometric exchange current density ($J_{0,geometric}$), double-layer capacitance (C_{dl}), relative electrochemically active surface area, normalized Tafel slope, and normalized exchange current density ($J_{0,normalized}$) of each electrode are summarized in Table 1. The normalized exchange current densities of NiP_2, $NiP_{1.93}Se_{0.07}$, $NiP_{0.09}Se_{1.91}$, and $NiSe_2$ were found to be 12, 31, 1.4, and 0.038 μA cm^{-2}, respectively. The doping of NiP_2 with Se significantly improved the HER performance as evidenced by the $J_{0,normalized}$ of $NiP_{1.93}Se_{0.07}$, which was 2.6 times larger than that of NiP_2, suggesting the higher intrinsic HER activity of $NiP_{1.93}Se_{0.07}$. The doping of NiP_2 with Se also reduced the Tafel slope (normalized) of NiP_2 from 51 to 43 mV $decade^{-1}$ (Figure 4d), which is desirable to drive a large catalytic current density at a low overpotential. Additionally, we found NiP_2 to be indeed catalytically more active than $NiSe_2$ for HER (although the Tafel slope for $NiSe_2$ is lower at 33 mV $decade^{-1}$). Although P-doping of $NiSe_2$ improved the catalytic performance, it could not surpass the performance of NiP_2 or Se-doped NiP_2. These results again confirm that the Se-doped NiP_2 ($NiP_{1.93}Se_{0.07}$) has the highest catalytic activity among these four compounds. The substitution of P by Se in the pyrite-phase NiP_2 is suggested to modify the electronic structure of NiP_2, which could further tune the hydrogen absorption free energy on the catalyst and improve the catalytic activity, as we have recently demonstrated for the analogous case of the pyrite-phase CoPS.[49] It is reasonable to speculate that higher percentage of substitution might lead to even better performance, however, as discussed above, we can not synthesize Se-doped NiP_2 with even higher Se percentage under this experimental

condition. Therefore, $NiP_{1.93}Se_{0.07}$ is practically the most active HER catalyst in the series of pure and doped pyrite-phase compounds from NiP_2 to $NiSe_2$.

Table 1. Summary of the electrochemical properties of NiP_2, $NiP_{1.93}Se_{0.07}$, $NiP_{0.09}Se_{1.91}$, and $NiSe_2$ on graphite disk (GD) and $NiP_{1.93}Se_{0.07}$ on carbon fiber paper (CP). The best values for each parameter among four samples on GD were highlighted with bold fonts.

Sample/Substrate	η (mV vs. RHE) for $J = -10$ mA cm^{-2}	**Tafel slope** (mV decade^{-1})	$J_{0,\text{geometric}}$ (μA cm^{-2})	C_{dl} (mF cm^{-2})	**Relative Surface Area**	**Tafel slope** $_{\text{normalized}}$ (mV decade^{-1})	$J_{0,\text{normalized}}$ (μA cm^{-2})
NiP_2/GD	135	48	15	8.96	1.84	51	12
$NiP_{1.93}Se_{0.07}$/GD	**102**	42	**39**	6.49	1.34	43	**31**
$NiP_{0.09}Se_{1.91}$/GD	167	44	1.4	4.86	1.00	44	1.4
$NiSe_2$/GD	173	**31**	0.031	7.35	1.51	**33**	0.038
$NiP_{1.93}Se_{0.07}$/CP	84	41	100	27.6	5.68	42	20

Furthermore, we measured the stability of the most catalytically active $NiP_{1.93}Se_{0.07}$ catalyst for HER (Figure 5). The electrode of $NiP_{1.93}Se_{0.07}$ nanostructures on graphite disk can maintain a current density of 10 mA cm^{-2} for ~14 h at an overpotential of 0.1 V (Figure 5a). The charge transfer resistance of the electrode only increased slightly from 4.5 Ω to 10 Ω (Figure 5b). The morphology of the microsctructure of $NiP_{1.93}Se_{0.07}$ changed very little after this 14 h test (Figure 5c). Also, the PXRD patterns of $NiP_{1.93}Se_{0.07}$ after the test show no significant changes (Figure 5d). These results demonstrate the excellent stability of $NiP_{1.93}Se_{0.07}$.

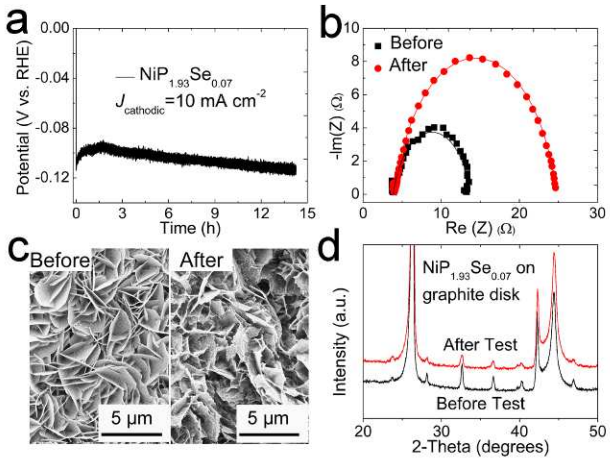

Figure 5. Characterization of stability of $NiP_{1.93}Se_{0.07}$ on graphite disk during HER electrocatalysis. (a) Long-term stability measurement holding the current density at 10 mA cm^{-2}, (b) Electrochemical impedance spectroscopy (EIS) Nyquist plots, (c) SEM images, and (d) PXRD patterns before and after the test.

Finally, to further improve the overall catalytic performance of $NiP_{1.93}Se_{0.07}$ for HER, we employed carbon fiber paper (CP), which has large surface area and good electrical conductivity, as the substrate to prepare high surface area three-dimensional (3D) electrodes in otherwise similar synthesis conditions. Figure 6 displays the SEM images, PXRD patterns, polarization curves, and the corresponding Tafel plot of $NiP_{1.93}Se_{0.07}$ nanostructures on carbon fiber paper. The $NiP_{1.93}Se_{0.07}$/CP electrodes achieved a catalytic current density of 10 mA cm^{-2} at an overpotential of 84 mV vs. RHE with a Tafel slope of 41 mV $decade^{-1}$. This catalytic activity is comparable to the most active HER catalysts in published results (see Table S1 in the Supporting Information).

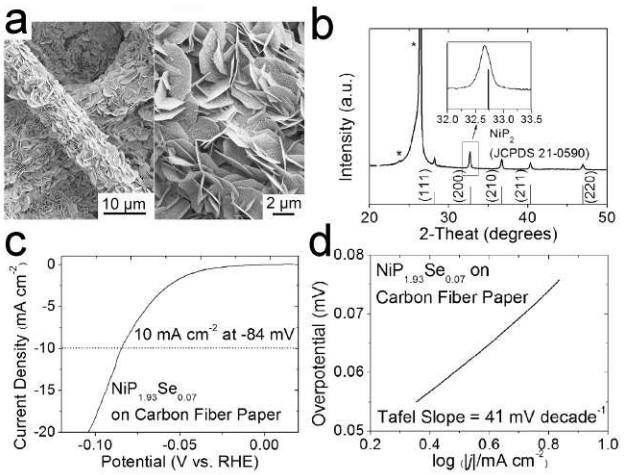

Figure 6. (a) SEM images, (b) PXRD patterns, (c) polarization curves and (d) the corresponding Tafel plot of $NiP_{1.93}Se_{0.07}$ nanostructures on carbon fiber paper.

CONCLUSIONS

In summary, we have developed a facile method to synthesize nanostructures of pyrite-phase NiP_2, nickel phosphoselenide ($NiP_{1.93}Se_{0.07}$, $NiP_{0.09}Se_{1.91}$), and $NiSe_2$. Their similar structures enable a systematic and fair comparison of their structural properties and catalytic activities for HER. Our results prove that Se-doped NiP_2 ($NiP_{1.93}Se_{0.07}$) exhibits the highest electrocatalytic activity among the four compounds. Specifically, $NiP_{1.93}Se_{0.07}$ nanostructures grown on carbon fiber paper achieved a current density of 10 mA cm^{-2} at – 84 mV (vs. RHE) with a small Tafel slope of 41 mV $decade^{-1}$. These results establish $NiP_{1.93}Se_{0.07}$ as a highly active, stable, and earth-abundant electrocatalyst for HER. Our work also demonstrates the significant influence of chemical composition modification (doping or alloying) of existing electrocatalysts on their catalytic activity, especially when doping with an anion from another group (e.g. selenium to phosphorus). This approach could be employed not only to design higher performance HER

catalysts, but also provides a general strategy to improve the intrinsic catalytic HER activity of the promising catalysts in the future.

ASSOCIATED CONTENT

AUTHOR INFORMATION

Corresponding Author

*Email: lmwx@pku.edu.cn

*Email: jin@chem.wisc.edu

Notes

The authors declare no competing financial interest.

ACKNOWLEDGMENT

This research is supported by the U.S. Department of Energy, Office of Basic Energy Sciences, Division of Materials Sciences and Engineering, under Award DE-FG02-09ER46664. S.J. also thanks UW-Madison H. I. Romnes Faculty Fellowship for support. J.Z. and H.L. thank the China Scholarship Council (CSC) for support. M.C.A. and L.S. thank NSF Graduate Research Fellowship for support. M.L. thanks the National Natural Science Foundation of China (grant no. 21275010) for support.

Supporting Informantion

The details of substrate preparation; the estimation of catalytic turnover frequency (TOF); the illustration of the autoclave apparatus; the Randles equivalent circuit used to fit the arcs in the

EIS spectra; SEM images and PXRD patterns of the $Ni(OH)_2 \cdot 0.75H_2O$ and $NiP_{2-x}Se_x$; EDS elemental mapping images of NiP_2, $NiP_{1.93}Se_{0.07}$, $NiP_{0.09}Se_{1.91}$, and $NiSe_2$; comparison of HER activity of some previously reported catalysts. This material is available free of charge via the Internet at http://pubs.acs.org.

REFERENCES

(1) Turner, J. A. *Science* **2004**, *305*, 972-974.
(2) Lewis, N. S., Nocera, D. G. *Proc. Natl. Acad. Sci. U. S. A.* **2006**, *103*, 15729-15735.
(3) Gray, H. B. *Nat. Chem.* **2009**, *1*, 7-7.
(4) Nocera, D. G. *Acc. Chem. Res.* **2012**, *45*, 767-776.
(5) Walter, M. G.; Warren, E. L.; McKone, J. R.; Boettcher, S. W.; Mi, Q.; Santori, E. A.; Lewis, N. S. *Chem. Rev.* **2010**, *110*, 6446-6473.
(6) Faber, M. S.; Jin, S. *Energy Environ. Sci.* **2014**, *7*, 3519-3542.
(7) Zeng, M.; Li, Y. *J. Mater. Chem. A* **2015**, *3*, 14942-14962.
(8) Vesborg, P. C. K.; Seger, B.; Chorkendorff, I. *J. Phys. Chem. Letter* **2015**, *6*, 951-957.
(9) Morales-Guio, C. G.; Stern, L. A.; Hu, X. *Chem. Soc. Rev.* **2014**, *43*, 6555-6569.
(10) Li, Y.; Wang, H.; Xie, L.; Liang, Y.; Hong, G.; Dai, H. *J. Am. Chem. Soc.* **2011**, *133*, 7296-7299.
(11) Morales-Guio, C. G.; Hu, X. *Acc. Chem. Res.* **2014**, *47*, 2671-2681.
(12) Vrubel, H.; Merki, D.; Hu, X. *Energy Environ. Sci.* **2012**, *5*, 6136-6144.
(13) Wang, T.; Liu, L.; Zhu, Z.; Papakonstantinou, P.; Hu, J.; Liu, H.; Li, M. *Energy Environ. Sci.* **2013**, *6*, 625-633.
(14) Voiry, D.; Yamaguchi, H.; Li, J.; Silva, R.; Alves, D. C.; Fujita, T.; Chen, M.; Asefa, T.; Shenoy, V. B.; Eda, G.; Chhowalla, M. *Nat. Mater.* **2013**, *12*, 850-855.
(15) Benck, J. D.; Hellstern, T. R.; Kibsgaard, J.; Chakthranont, P.; Jaramillo, T. F. *ACS Catal.* **2014**, *4*, 3957-3971.
(16) Cheng, L.; Huang, W.; Gong, Q.; Liu, C.; Liu, Z.; Li, Y.; Dai, H. *Angew. Chem., Int. Ed.* **2014**, *53*, 7860-7863.
(17) Lukowski, M. A.; Daniel, A. S.; English, C. R.; Meng, F.; Forticaux, A.; Hamers, R. J.; Jin, S. *Energy Environ. Sci.* **2014**, *7*, 2608-2613.
(18) Lukowski, M. A.; Daniel, A. S.; Meng, F.; Forticaux, A.; Li, L.; Jin, S. *J. Am. Chem. Soc.* **2013**, *135*, 10274-10277.
(19) Faber, M. S.; Dziedzic, R.; Lukowski, M. A.; Kaiser, N. S.; Ding, Q.; Jin, S. *J. Am. Chem. Soc.* **2014**, *136*, 10053-10061.
(20) Faber, M. S.; Lukowski, M. A.; Ding, Q.; Kaiser, N. S.; Jin, S. *J. Phys. Chem. C* **2014**, *118*, 21347-21356.
(21) Kong, D.; Cha, J. J.; Wang, H.; Lee, H. R.; Cui, Y. *Energy Environ. Sci.* **2013**, *6*, 3553-3558.
(22) Kong, D.; Wang, H.; Lu, Z.; Cui, Y. *J. Am. Chem. Soc.* **2014**, *136*, 4897-4900.
(23) Wu, X.; Yang, B.; Li, Z.; Lei, L.; Zhang, X. *RSC Adv.* **2015**, *5*, 32976-32982.
(24) Saadi, F. H.; Carim, A. I.; Velazquez, J. M.; Baricuatro, J. H.; McCrory, C. C. L.; Soriaga, M. P.; Lewis, N. S. *ACS Catal.* **2014**, *4*, 2866-2873.
(25) Kong, D.; Wang, H.; Cha, J. J.; Pasta, M.; Koski, K. J.; Yao, J.; Cui, Y. *Nano Lett.* **2013**, *13*, 1341-1347.
(26) Carim, A. I.; Saadi, F. H.; Soriaga, M. P.; Lewis, N. S. *J. Mater. Chem. A* **2014**, *2*, 13835-13839.
(27) Gong, F.; Xu, X.; Li, Z.; Zhou, G.; Wang, Z. S. *Chem. Commun.* **2013**, *49*, 1437-1439.
(28) Zhang, H.; Yang, B.; Wu, X.; Li, Z.; Lei, L.; Zhang, X. *ACS Appl. Mater. Interfaces* **2015**, *7*, 1772-1779.
(29) Liang, H.; Li, L.; Meng, F.; Dang, L.; Zhuo, J.; Forticaux, A.; Wang, Z.; Jin, S. *Chem. Mater.* **2015**, *27*, 5702-5711.
(30) Chen, W. F.; Muckerman, J. T.; Fujita, E. *Chem. Commun.* **2013**, *49*, 8896-8909.

(31) Cao, B.; Veith, G. M.; Neuefeind, J. C.; Adzic, R. R.; Khalifah, P. G. *J. Am. Chem. Soc.* **2013**, *135*, 19186-19192.
(32) Popczun, E. J.; Read, C. G.; Roske, C. W.; Lewis, N. S.; Schaak, R. E. *Angew. Chem., Int. Ed.* **2014**, *53*, 5427-5430.
(33) Feng, L.; Vrubel, H.; Bensimon, M.; Hu, X. *Phys. Chem. Chem. Phys.* **2014**, *16*, 5917-5921.
(34) Wang, T.; Du, K.; Liu, W.; Zhu, Z.; Shao, Y.; Li, M. *J. Mater. Chem. A* **2015**, *3*, 4368-4373.
(35) Popczun, E. J.; McKone, J. R.; Read, C. G.; Biacchi, A. J.; Wiltrout, A. M.; Lewis, N. S.; Schaak, R. E. *J. Am. Chem. Soc.* **2013**, *135*, 9267-9270.
(36) Kibsgaard, J.; Jaramillo, T. F. *Angew. Chem., Int. Ed.* **2014**, *53*, 14433-14437.
(37) Jiang, P.; Liu, Q.; Sun, X. *Nanoscale* **2014**, *6*, 13440-13445.
(38) Xiao, P.; Sk, M. A.; Thia, L.; Ge, X.; Lim, R. J.; Wang, J.-Y.; Lim, K. H.; Wang, X. *Energy Environ. Sci.* **2014**, *7*, 2624-2629.
(39) Callejas, J. F.; McEnaney, J. M.; Read, C. G.; Crompton, J. C.; Biacchi, A. J.; Popczun, E. J.; Gordon, T. R.; Lewis, N. S.; Schaak, R. E. *ACS Nano* **2014**, *8*, 11101-11107.
(40) McEnaney, J. M.; Crompton, J. C.; Callejas, J. F.; Popczun, E. J.; Biacchi, A. J.; Lewis, N. S.; Schaak, R. E. *Chem. Mater.* **2014**, *26*, 4826-4831.
(41) McEnaney, J. M.; Crompton, J. C.; Callejas, J. F.; Popczun, E. J.; Read, C. G.; Lewis, N. S.; Schaak, R. E. *Chem. Commun.* **2014**, *50*, 11026-11028.
(42) Hansen, M. H.; Stern, L. A.; Feng, L.; Rossmeisl, J.; Hu, X. *Phys. Chem. Chem. Phys.* **2015**, *17*, 10823-10829.
(43) Scanlon, M. D.; Bian, X.; Vrubel, H.; Amstutz, V.; Schenk, K.; Hu, X.; Liu, B.; Girault, H. H. *Phys. Chem. Chem. Phys.* **2013**, *15*, 2847-2857.
(44) Vrubel, H.; Hu, X. *Angew. Chem., Int. Ed.* **2012**, *51*, 12703-12706.
(45) Faber, M. S.; Park, K.; Cabán-Acevedo, M.; Santra, P. K.; Jin, S. *J. Phys. Chem. Letter* **2013**, *4*, 1843-1849.
(46) Karunadasa, H. I.; Montalvo, E.; Sun, Y.; Majda, M.; Long, J. R.; Chang, C. J. *Science* **2012**, *335*, 698-702.
(47) Jaramillo, T. F.; Jorgensen, K. P.; Bonde, J.; Nielsen, J. H.; Horch, S.; Chorkendorff, I. *Science* **2007**, *317*, 100-102.
(48) Kibsgaard, J.; Jaramillo, T. F.; Besenbacher, F. *Nat. Chem.* **2014**, *6*, 248-253.
(49)Cabán-Acevedo, M.; Stone, M. L.; Schmidt, J. R.; Thomas, J. G.; Ding, Q.; Chang, H. C.; Tsai, M. L.; He, J. H.; Jin, S. *Nat. Mater.* **2015**, DOI: http://dx.doi.org/10.1038/nmat4410.
(50) Doxohue, P. C.; Bither, T. A.; Young, H. S. *Inorg. Chem.* **1968**, *7*, 998-1001.
(51) Kucernak, A. R. J.; Sundaram, V. N. N. *J. Mater. Chem. A* **2014**, *2*, 17435-17445.
(52) Wang, D. Y.; Gong, M.; Chou, H. L.; Pan, C. J.; Chen, H. A.; Wu, Y.; Lin, M. C.; Guan, M.; Yang, J.; Chen, C. W.; Wang, Y. L.; Hwang, B. J.; Chen, C. C.; Dai, H. *J. Am. Chem. Soc.* **2015**, *137*, 1587-1592.
(53) Gong, Q.; Cheng, L.; Liu, C.; Zhang, M.; Feng, Q.; Ye, H.; Zeng, M.; Xie, L.; Liu, Z.; Li, Y. *ACS Catal.* **2015**, *5*, 2213-2219.
(54) Zhang, X.; Meng, F.; Mao, S.; Ding, Q.; Shearer, M. J.; Faber, M. S.; Chen, J.; Hamers, R. J.; Jin, S. *Energy Environ. Sci.* **2015**, *8*, 862-868.
(55) Xu, K.; Wang, F.; Wang, Z.; Zhan, X.; Wang, Q.; Cheng, Z.; Safdar, M.; He, J. *ACS Nano* **2014**, *8*, 8468-8476.
(56) Xia, X.; Chao, D.; Qi, X.; Xiong, Q.; Zhang, Y.; Tu, J.; Zhang, H.; Fan, H. J. *Nano Lett.* **2013**, *13*, 4562-4568.
(57) Foecker, A. J.; Jeitschko, W. *J. Solid State Chem.* **2001**, *162*, 69-78.
(58) Vogt, H.; Chattopadhyay, T.; Stolz, H. J. *J. Phys. Chem. Solids* **1983**, *44*, 869-873.
(59) Cabán-Acevedo, M.; Kaiser, N. S.; English, C. R.; Liang, D.; Thompson, B. J.; Chen, H. E.; Czech, K. J.; Wright, J. C.; Hamers, R. J.; Jin, S. *J. Am. Chem. Soc.* **2014**, *136*, 17163-17179.
(60) Merki, D.; Vrubel, H.; Rovelli, L.; Fierro, S.; Hu, X. *Chem. Sci.* **2012**, *3*, 2515.

Table of Contents Graphic